Topography and the global overturning: The changing impact of small scale effects with resolution.

Maike Sonnewald*

Massachusetts Institute of Technology, 77 Massachusetts Ave, Cambridge, MA 02139, USA, Harvard University, 26 Oxford Street, Cambridge, MA 02138, USA and The University of Texas at Austin, 201 East 24th Street, Austin, TX 78712,USA

Joël J-.M. Hirschi, A. George Nurser, Andrew Coward &

National Oceanography Centre, Southampton,European Way, Southampton SO14 3ZH, UK

Patrick Hyder

Met Office, FitzRoy Road, Exeter EX1 3LX, UK

**Corresponding author address:* Maike Sonnewald, Massachusetts Institute of Technology, 77 Massachusetts Ave, Cambridge, MA 02139, USA.

E-mail: maike_s@mit.edu

ABSTRACT

Ocean physics are an integral part of the climate, and being able to model them with confidence is key to preempting future change. Theoretical understanding of ocean physics is largely based on a laminar view of the ocean, assuming the non-linear vorticity terms are small. Here we investigate the changing interaction with topography through the bottom pressure torque term, and how it impacts the global overturning. A coarse (1°), an eddy permitting (1/4°) and an eddy resolving (1/12°), version of the NEMO general circulation model is used. The 30-year mean shows that the baroclinic contribution to ocean heat transport becomes increasingly important with higher resolution, especially in the Southern Ocean. This implies that resolving eddies leads to a shift in the balance of forces and to a different partitioning of the ocean heat transport. Using the depth integrated vorticity equation, the shift is ascribed to eddy contributions to bottom steering in the bottom pressure torque term. This suggests a fundamental change in how the circulation is realized, with important implications for the fidelity and utility of ocean modeling efforts.

1. Motivation

Profound changes are demonstrated in numerical ocean model interaction with topography when increasing horizontal resolution. Understanding the topographic influence on the global overturning is key to determining how and where the small scale contribution is significant. The small scale effects are highly sensitive to how well resolved the topography is and how well developed the eddy field is. Determining changes in dynamics associated specifically with horizontal resolution highlights where and why the additional computational effort is justified. Moving from a coarse (non eddy-resolving), intermediate (eddy permitting), and high (eddy resolving) model, the eddy driven, baroclinic, component of the circulation becomes increasingly important. A profound change in the energy partitioning implies a change in ocean dynamics, that imprints itself on the global overturning circulation. Focusing explicitly on changes with horizontal resolution, the direct impact on the large scale circulation is systematically assessed. Interactions with bathymetry are particularly interesting in the Southern Ocean, as the circulation lacks a western boundary to supply the friction to balance the wind stress (Munk and Palmén 1951). The lack of continuous meridional barriers in the Southern Ocean lead to the conventionally accepted conjecture that baroclinic eddy activity accounts for meridional transport.

Increasing the horizontal resolution of an ocean model is associated with increased accuracy, and encouraged by groups such as the IPCC (IPCC 2013). Results demonstrating increasing accuracy with higher resolution are not uncommon (Megann *et al.* 2014; Marzocchi *et al.* 2015). Marsh *et al.* (2009) illustrate a better fit to the RAPID mooring array observations when resolving eddies, and reduced bias in climate models was demonstrated by Scaife *et al.* (2011). This could suggest that predictive power can be gained by explicitly resolving more processes such as eddies and associated interactions (Yeager 2015).

The large scale circulation can be understood in terms of an acceleration due to wind stress (τ_w), and a deceleration due to pressure forces exerted by bathymetry ($p_b \nabla H$) (Sverdrup 1947; Stommel and Arons 1960a,b). The ∇H term changes when the horizontal resolution is increased. This is seen invoking the steady, depth-integrated momentum equation following Hughes and de Cuevas (2001); Naveira Garabato *et al.* (2013):

$$f\mathbf{k} \times \mathbf{U} + \nabla P = p_b \nabla H + \tau_w - \tau_b - \mathbf{R}, \tag{1}$$

where f is the Coriolis parameter, $\mathbf{k}$ is the vertical upwards unit vector, $\mathbf{U} = \int_{-H}^{\eta} \rho \mathbf{u}$ represents the depth integrated mass transport (where H is the depth of the ocean and η the height of the surface, ρ is the density and $\mathbf{u}$), $P = \int_{-H}^{\eta} p dz$ is the depth integrated pressure (p), p_b is the bottom pressure, τ_b are the bottom friction forces (drag). $\mathbf{R}$ is the collection of contributions to the lateral redistribution of momentum by nonlinearities and lateral viscous stresses. $\mathbf{R}$ can be shown to be negligible if a large enough area is considered, but may be significant locally (Hughes and de Cuevas 2001; Naveira Garabato *et al.* 2013). The thermal wind is forced locally by τ_w, and balanced by τ_b and pressure sources on bathymetry. The sensitivity to resolution is highlighted in the $p_b \nabla H$ term.

Interactions between steep and sloping bathymetry and the circulation impact the vorticity balance, with the deep flow associated with the heat flux forcing (Yeager 2015; Luyten *et al.* 1985). Studies by Schoonover *et al.* (2016); Yeager (2015); Hughes and de Cuevas (2001); Jackson *et al.* (2006); Wells and de Cuevas (1995) highlight the role of bottom pressure torque in balancing the wind stress, in opposition to the classical models of Stommel (1948); Munk

(1950). The importance of abyssal flow interactions with bathymetry has implications for modeling efforts, as the ∇H term changes with resolution. Modeling choices of resolution and parameterization are seen to impact the nature of how the ocean realizes its circulation, and achieving good representations of frictional and viscous effects (both explicit and numerical) is important for key features such as the western boundary current (WBC) separation and the global overturning (Yeager 2015; Schoonover *et al.* 2016).

The lack of western boundaries implies that the Southern Ocean is governed by another mechanism, and no simple linear model has gained acceptance in literature (LaCase and Isachsen 2010). Munk and Palmén (1951) suggest that the wind stress is balanced by bottom friction, as the ACC interacts with topography in key regions. As Wells and de Cuevas (1995) discuss, the stratification and explicit representation of eddies is important for the vertical transport of stress from the surface, and the creation of the bottom form drag. The meridional components of the current make it span sufficient depth to allow a communication of stresses from surface to bottom. The mechanism suggested by Munk and Palmén (1951) would be highly sensitive to changes in the horizontal resolution through changes in the ∇H as well as the surface to depth communication enabled by resolving smaller scales.

The role of topography in the overturning and gyre circulation was demonstrated by Yeager (2015) in the North Atlantic in a realistic numerical model. Using a barotropic vorticity framework, the role of topography through ∇H is expressed as the torque associated with the bottom pressure (BPT). Yeager (2015) shows that the BPT plays a fundamental role in the overturning and gyre circulation, as well as the large-scale barotropic and baroclinic flows.

Here, the global ocean is considered at coarse (non-eddy resolving 1°), intermediate (eddy permitting 1/4°), and high (eddy resolving 1/12°) resolution, where the suite of ocean model runs are kept as close together as possible, unsing the same surface forcing and only changing parameters to preserve numerical stability. The change in topographic interaction is assessed, with particular focus on the baroclinic component of the BPT. The paper is organized as follows: Section 2 we present methods and theory. Section 3 presents the results, while section 4 concludes the paper with a discussion and outlook.

2. Modeling and theoretical framework

The Nucleus for European Modelling of the Ocean (NEMO, Madec (2008) in the ORCA configuration) over 30 years (1978 to 2007) is used. The z-level model and uses an Arakawa C-grid with 75 vertical levels and horizontal resolution ranging from 1° (ORCA1), 1/4° (ORCA025) and 1/12° (ORCA0083). The suite of runs is kept as similar as possible, while conserving numerical stability. A leapfrog timestepping scheme is used to reduce noise (Arakawa and Lamb 1977). The surface layer is allowed to vary and we use a non-linear free surface scheme. The equation of state used is Jackett and McDougall (1995). Analysis is performed on 5 day averages, while the timestep in the model forcing is 6 hourly using the forcing DFS4.1 (Brodeau *et al.* 2010) for all three runs. The ice model is the LIM sea-ice model. Tides and geothermal heating are not included, but a diffusive, nonlinear friction, bottom boundary layer scheme is active. The bottom diffusivity parameters stay constant at 1000 $m^2 s^{-1}$ in the different resolutions. Further, noise is reduced using an energy-enstrophy conserving scheme for momentum advection in combination with using partial cells at the bottom. The bathymetry of the 1°, 1/4° to 1/12° are described in

Coward (2006), Barnier *et al.* (2006) and Bourdallé-Badie *et al.* (2012), respectively.

Table 1 lists key parameters that change with the resolution. At 1° ORCA1, the addition of GM, calculated from the local growth rate of baroclinic instabilities, acts to adjust the advective formulation. The horizontal laplacian eddy viscosity decreases from $1.25 \times 10^{10} m^4 s^{-1}$ in ORCA1 to $500 m^4 s^{-1}$ in ORCA025 and ORCA0083. The horizontal bilaplacian eddy viscosity decreases from $1.25 \times 10^{10} m^4 s^{-1}$ in ORCA1 to $2.2 \times 10^{11} m^4 s^{-1}$ in ORCA025 and ORCA0083. The lateral eddy tracer diffusivity decreases consistently from $10^3 m^2 s^{-1}$ in ORCA1 to $300 m^2 s^{-1}$ in ORCA025 and $125 m^2 s^{-1}$ in ORCA0083. Parameters associated with the turbulent kinetic energy (TKE) scheme, Richardson number dependent vertical diffusion or vertical physics do not change with resolution because the vertical resolution does not change. However, these are velocity dependent, and may behave differently between resolutions even though the parameters are kept fixed.

Assessing changes in the global circulation, the overturning streamfunction (Ψ) in density space (σ, referenced to 2000m) is used as described in Zika *et al.* (2012); Nurser and Lee (2004).

$$\Psi_{\sigma y} = \frac{1}{\Delta t} \int_t^{t+\Delta t} \int \int_{\sigma' \leq \sigma} v dx dz dt. \quad (2)$$

Ψ is decomposed into barotropic (BT: $\overline{v}$) and baroclinic (BC: v') components:

$$\Psi_{\sigma y}^{BC} = \int \int_{\sigma' \leq \sigma} v' dxdz,$$
$$\Psi_{\sigma y}^{BT} = \int \int_{\sigma' \leq \sigma} \overline{v} dxdz, \tag{3}$$
$$\Psi_{\sigma y} = \Psi_{\sigma y}^{BC} + \Psi_{\sigma y}^{BT}.$$

Where $v = \overline{v} + v'$, and $\overline{v} = \frac{1}{H} \int_z^0 v dz$ and v_{BT} is the remainder.

Moving from the barotropic momentum equation to the as barotropic vorticity equation is demonstrated by Hughes and de Cuevas (2001); Yeager (2015); Schoonover *et al.* (2016). Due to the BPT term's sensitivity to topographic roughness, it is worth developing a physical intuition for the interpretation of the term. Under a geostrophic scaling, the BPT can be interpreted as vortex tube stretching. Following Cane *et al.* (1998), forming a vorticity equation and then vertically integrating:

$$\beta \psi_x = -f w_b + \mathbf{k} \cdot \nabla \times \frac{\tau_w}{\rho_0} + R. \tag{4}$$

The transport streamfunction ψ is the depth integrated stream function, and w_b is the vertical component velocity at the ocean floor:

$$w_b = u_b \cdot \nabla(H) = \frac{1}{\rho_0 f} J(p, H)|_b. \tag{5}$$

The subscript b indicates the term is evaluated at the bottom, and u_b is the horizontal *geostrophic* velocity at the sea floor, and the final relation is a consequence of geostrophy. J is the Jacobian defined as: $J(u, v) = u_x v_y - u_y v_x$.

Note that mathematically, the $J(p,H)|_b$ is equivalent to the more familiar $J(p_b,H)$ according to:

$$J(p_b,H) = \frac{\partial p_b}{\partial x}\frac{\partial H}{\partial y} - \frac{\partial p_b}{\partial y}\frac{\partial H}{\partial x} = J(p,H)_b, \tag{6}$$

where p_b is the pressure evaluated at the bottom ($z = -H$), since:

$$\begin{aligned} \frac{\partial p_b}{\partial x} &= \left.\frac{\partial p}{\partial x}\right|_z + \left.\frac{\partial p}{\partial z}\frac{z}{\partial x}\right|_z \\ &= \left.\frac{\partial p}{\partial x}\right|_z + \rho g\frac{\partial H}{\partial x}, \end{aligned} \tag{7}$$

and the equivalent term for $\frac{\partial p_b}{\partial y}$ cancel out.

Increasingly resolving small scale features of rough bathymetry (∇H), Cane *et al.* (1998); Yeager (2015) discuss how a uniform density ocean will have its inviscid flow constrained following geostrophic f/H contours (Pedlowski 1979). Barotropic flow will cross f/H contours to balance the vorticity input by the winds, implying an imprint on the overturning characteristics with changing model resolution. For a flat bottom, we would look at f contours. However, in NEMO, the realistic bathymetry offers very interesting H contours. These gradients in H imply interesting deep flow, and convergence/divergence in regions relative to pure β-effect regions. In this sense, we arrive at equation 5.

The theoretical link between the relief, bottom velocity and vortex stretching, motivates an assessment of BPT and its baroclinic component; the Joint Effect of Baroclinicity and Relief (JEBAR). The BPT arises in the vorticity equation of vertically integrated horizontal velocity, while the Joint Effect of Baroclinicity and Relief (JEBAR) term arises from the vertically-averaged horizontal velocity (Yeager 2015; Bell 1999; Greatbatch *et al.* 1991; Mertz and Wright 1992).

In this manner, JEBAR represents the BPT component that is associated with the buoyancy dependent and baroclinic part of the pressure gradient, vanishing in the absence of stratification.

Expressing the BPT in terms of the barotropic depth averaged flow:

$$\frac{1}{\rho_0}J(p_b,H) = f\mathbf{u}_{gb}\cdot\nabla H = \overbrace{f(\mathbf{u}_{gb}-\overline{\mathbf{u}}_g)\cdot\nabla H}^{\text{Baroclinic}} + \overbrace{f\overline{\mathbf{u}}_g\cdot\nabla H}^{\text{Barotropic}}. \tag{8}$$

Mertz and Wright (1992) highlight that the expression for BPT is the sum of a baroclinic (JEBAR) and barotropic component. Appendix A1 details moving from the geostrophic balance in the meridional momentum equation to find the JEBAR term as $\frac{1}{H}J(\Phi,H)$, where Φ is the potential energy per unit area: $\Phi = \frac{g}{\rho_0}\int_{-H}^{0} z\rho dz$.

Substituting 8 into the vorticity equation 4, and introducing Ψ, we find that:

$$\beta\frac{\partial\Psi}{\partial x} = \frac{1}{H}J(\Phi,H) + f\overline{\mathbf{u}}_g\cdot\nabla H + \frac{1}{\rho_0}[\mathbf{k}\cdot\nabla\times\tau]. \tag{9}$$

Then:

$$H\overline{\mathbf{u}}_g + \frac{\mathbf{k}\times\tau}{\rho_0 f} = H\overline{\mathbf{u}}_{total}. \tag{10}$$

It follows that:

$$\begin{aligned}
\beta\frac{\partial\Psi}{\partial x} &= \frac{1}{H}J(\Phi,H) + \frac{f}{H}J(\Psi,H) + H\rho_0^{-1}\mathbf{k}(\nabla\times\frac{\tau}{H}),\\
&\Rightarrow\frac{1}{H}J(\Psi,f) - \frac{f}{H^2}J(\Psi,H) = \frac{1}{H^2}J(\Phi,H) + \rho_0^{-1}(\mathbf{k}\cdot\nabla\times\frac{\tau}{H}),\\
&\Rightarrow\frac{1}{H}J\left(\Psi,\frac{f}{H}\right) = -J\left(\Psi,\frac{1}{H}\right) + \rho_0^{-1}(\mathbf{k}\cdot\nabla\times\frac{\tau}{H}).
\end{aligned} \tag{11}$$

Here the term $J(\Phi, \frac{1}{H})$ is the JEBAR term (Mertz and Wright 1992; Sarkisyan and Ivanov 1971).

There are several interpretations of this in the context of real ocean flows. Myers *et al.* (1996) suggests that it illustrates the difference between bottom pressure torque and the corresponding torque associated with depth averaged pressure, while Mertz and Wright (1992) also suggest it relates to bottom torque (as the curl of the horizontal force by the bottom of the fluid) but also that it can be seen as the geostrophic component of the correction to the topographic stretching term. This accounts for that it is in fact the bottom velocity, not the depth averaged velocity, which gives rise to the vortex-tube stretching.

Cane *et al.* (1998) points out that the utility of the JEBAR term is limited, as calculating it consistently is complicated by imperfect cancellation and spurious transport values. The calculated fields are noisy, and have large relative errors. The majority of ocean transports are confined to the surface, and the JEBAR term can overestimate the influence of topography on ocean transports. Meaning relative errors are important for the interpretation of results.

Objectively comparing the different runs is done using an area averaged probability distribution function (PDF):

$$PDF = lim_{\Delta\phi \to 0} \left(\int \int_{\phi_0 < \phi < \phi + \Delta\phi} dA \right) / \int \int dA. \tag{12}$$

Related to the the cumulative distribution function (CDF) according to $PDF = \frac{d}{d\phi} CDF$ and $CDF(\infty) = 1$, representing the probability of a value of ϕ occurring. The area associated with a certain range of a quantity of interest ϕ in summarized, and normalize by the total area of the ocean ($\int\int dA$) it represents.

3. Results

Figure 1 shows the 30 year time mean of the global overturning cell in density space as defined in equation 2. The lighter equatorial waters show the big wind-drived gyres, while waters get increasingly dense moving polewards, lending the figures the bell-shape. At $\approx 52°$N the North Atlantic deep water (NADW) is visible. Spreading form the high latitudes in the Southern Hemisphere the Antarctic bottom water (AABW) spreads northward. The deep circulation in the Southern Ocean and its northward extension, as well as the NADW cell, are significantly strengthened with increasing resolution. The equatorial and subtropical cells are strikingly similar, and intensify with increasing resolution.

Following equation 3 the 30 year time mean overturning $\Psi_{\sigma y}$ is decomposed into barotropic and baroclinic components in figure 2. The barotropic component is seen to often counter the direction of the baroclinic, with the opposite signs leading to compensating transports. Absolute overturning values are markedly smaller for the full overturning than for the barotropic and baroclinic components. The baroclinic component contains the wind driven gyre feature in the lighter, low latitude waters, as well as the clockwise component of the NADW. The anti-clockwise component in the Southern Ocean is primarily found in the baroclinic component. The make up of AABW and NADW cells change with latitude with e.g. the northernmost part of the NADW cell being dominated by the baroclinic component, whilst further south (between 20-40°N) the barotropic component dominates. Figure 2 illustrates that the increase in anti-clockwise circulation in the Southern Ocean can be accounted for by the baroclinic circulation. We see a clockwise dense circulation in the Southern Ocean in the barotropic mean, extending northward and into lighter water masses with increasing resolution. Overall, in the subtropics, we see a strengthening of the subtropical circulation with decreasing resolution. However, the anti-clockwise WBCs become increasingly well defined with resolution in the Southern Hemisphere. Further changes in the Northern Hemisphere include a strengthening of the NADW with resolution, and a weakening of the baroclinic anti-clockwise subtropical circulation. In the baroclinic mean, the clockwise WBCs in the Northern Hemisphere become better defined and span a wider range of densities with increasing resolution.

Figure 3 highlights the change in the ∇H term with resolutions. The shelf is outlined around the continents, especially in the low resolution ORCA1. Vast expanses of ocean bathymetry appear smooth in low resolution ORCA1, in contrast to intermediate ORCA025 and high resolution ORCA0083. We can see the outline of the Atlantic Ridge, as well as the Pacific-Antarctic and the Southwest Indian Ridge. The fracture zones in the Southern Ocean are visible as orthogonal streaks to the ridge structures, specifically the Eltanin and Udintsev fracture zones on the Pacific-Antarctic Ridge. We see that the Drake Passage and Scotia Ridge area are associated with dramatic bathymetry, with increasing steepness with resolution. The Weddell Gyre region can be seen as a reasonably cut-off area in terms of bathymetry. For ORCA025 more detail appears in ∇H, features are visible in the interior particularily over regions of known rough bathymetry. In ORCA0083 there is a marked increase in roughness, with isolated “hotspots”.

The roughness information in figure 3 can be summarized using probability distribution functions in figure 4 as defined in equation 12. This is done for the global as well as the longitudinal averages. All resolutions demonstrate that most of the ocean floor is fairly smooth, with low values of ∇H dominating spatially. The steep slopes tend to cluster around discrete values, which illustrates that the slopes are largely similar irrespective of the basin. Steeper slopes are found with increasing resolution as expected; ORCA0083 clusters around higher values, a tendency which increases towards the higher latitudes. This is expected due to the higher number of gridpoints. ORCA025 also has higher values, but more concentrated towards lower bins. In the plots of longitudinal averages there are streaks of higher probability which are set by the resolution, changing with latitude. This can be seen in the equatorial region of ORCA1 where the tropical mesh refinement increases the resolution smoothly to 1/3°.

Figure 5 is the 30 year mean BPT. Figure 5a for ORCA1 shows that the strongest BPT are found in the shelf regions and regions of steep bathymetry, such as the Scotia Ridge, the Kerguelen Plateau and the Northern Mid-Atlantic Ridge. A physically intuitive pattern of positive (negative) BPT to the East of a topographic feature, and negative (positive) to the West for eastward (westward) flow. This can be interpreted as the flow converging as it hits the obstacle and diverging after, leading to vortex squishing initially, and vortex stretching after.

Figure 5b shows the 30 year mean BPT for ORCA025. Patterns are similar to ORCA1, but regions are locally more confined to smaller areas on the shelf. Similar structures of negative/positive values in response to topographic berriers are seen. Areas where the BPT is significant are more widespread, and the Northern Mid-Atlantic Ridge down to the Equator, as well as the Pacific-Antarctic Ridge and the East Pacific Ridge stand out.

The high resolution ORCA0083 30 year mean BPT is shown in figure 5c. The patterns seem noisy, in sharp contrast to ORCA1 and ORCA025. The pattern of negative/positive values persist, and again this is locally quite confined. The ridge structures are less clearly defined, and many more areas are seen to incur BPT responses. Some features are also more pronounced, with the South-West Indian Ridge and Atlantic-Indian Ridge standing out as extensions of the Scotia Ridge after the Drake Passage.

The BPT changes significantly with changing horizontal resolution, moving away from clearly confined shelf features through a clearer influence of even deeper bathymetry and finally to a more stochastic but spatially connected picture.

Figure 6 shows the PDFs of the 30 year mean of the BPT in figure 5. ORCA1 is more noisy than ORCA025 and ORCA0083, with the distribution becoming smoother with increasing resolution likely due to the increased number of gridcells. This is particularly evident in the global average. A slight increase in the Southern Ocean BPT is highlighted with increasing resolution, with ORCA0083 having higher values. The area averaging that takes place to fairly compare the BPT of the changing resolution dampens much of the signal.

To elucidate the relevant, baroclinic, component of the BPT term, the JEBAR term is shown in Figure 7 for the 30 year mean. The JEBAR term is expected to be larger where we have sharper gradients of H interacting with stratified flow. This type of interaction is found specifically on the shelf break and in areas of sharp ∇H.

Figure 7a illustrates that in ORCA1 most of the activity is confined to the shelves for the 30 year mean JEBAR term. Figure 7b shows a pattern more similar to the BPT for the 30 year mean JEBAR term in ORCA025, where bathymetric features stand out but are less clearly partitioned with positive/negative features aligned with the mean flow. Figure 7c shows the JEBAR term for the 30 year mean in ORCA0083, which has an even more pronounces "noisy" JEBAR term. The bathymetric features stand out, but without the more coherent patterns of negative/positive BPT. Features such as the Pacific-Antarctic Ridge in the Pacific sector of the Southern Ocean. We see features like the Scotia Ridge clearly in all resolutions, but we see that the influence of the region is increasingly visible with increasing resolution. In ORCA0083 we can already pick out features like the mid-Atlantic Ridge and various fracture zones.

To elucidate the seemingly "noisy" JEBAR term, figure 8 shows a detail from northern Japan in the Kamtchatka region for ORCA1 in figure 8a, and ORCA0083 in figure 8b. This highlights the increased intricacy of the flow patterns that the decreased viscosity allows in ORCA0083. Coherent regions where the JEBAR term is important are seen in ORCA0083. The large scale patterns are preserved in ORCA1, but large sections have a little or no impact on the JEBAR term.

Certain regions have a negative/positive pattern, making it plausible that the effects of increasing resolution would average out with coarsegraining. However, figure 9 demonstrates that this is not the case. The global average PDF illustrates that ORCA0083 is profoundly different than ORCA1, with the intermediate resolution ORCA025 somewhere in the middle. The changes in JEBAR highlight the barotropic component of the BPT compensation, that we expected from the baroclinic and barotropic components of the overturning streamfunction (Figure 2). This is evident from the changes in the PDFs in figure 9, and we see that this is particularly the case in regions such as the Southern Ocean.

4. Discussion and conclusions

The effect of abyssal small scale topography on the global overturning is examined through varying horizontal resolution. Increasing horizontal resolution leads to a strengthening in the counter clockwise dense water circulation in the Southern Ocean. Using a decomposition into the barotropic and baroclinic contributions to the overturning, the complex feedback between the components that make up the global overturning is demonstrated. The baroclinic anti-clockwise component is largely compensated by the barotropic clockwise overturning in the Southern Ocean. The Southern Ocean is uniquely suited as a case study, as eddy processes are particularly important; topography is critical due to a lack of western boundaries, and varying horizontal resolution allows a direct assessment of this effect. This is captured specifically by the BPT term. There is an increase in the interaction of the baroclinic component with topograpy (JEBAR) with increasing horizontal model resolution. This is consistent with the increase in overturning found for higher resolutions.

Munk and Palmén (1951) were one of the first to highlight the Southern Ocean as a unique place in the ocean, where no western boundary continents supply sufficient friction to balance the wind stress. This implies that the Southern Ocean is governed by another mechanism to balance forces. Munk and Palmén (1951) suggest that the wind stress is balanced by bottom friction where the ACC interacts with topography, with the meridional components of the current making it span sufficient depth to allow this communication of stresses from surface to bottom. There is increased communication between the surface and deep ocean, as well as an increasing tendency towards barotropic columns in the higher resolution. This suggests that the mechanism suggested by Munk and Palmén (1951) would be highly sensitive to changes in the horizontal resolution.

Penduff *et al.* (2002) illustrate that smoothing the topography has a large effect on eddy flows, suggesting that changing ∇H could have large impacts. For all resolutions, the BPT term is similar for both the monthly mean field (not shown) and the 30 year mean. The effect of smoothing the bathymetry, but keeping the resolution the same in Penduff *et al.* (2002) confirms that the distribution of baroclinic work towards realising the overturning is sensitive to ∇H, rather than simply being reflected in the PBT term.

Wells and de Cuevas (1995) explore momentum balance in the Southern Ocean, exploring the role of BPT but not the horizontal resolution. Here the wind stress term and the beta term are thought to dominate. They point out that the wind stress term is an order of magnitude smaller unless a zonal integral along streamlines is considered. This is because the sign of the wind remains constant, while other terms like the lateral friction have varying sign. They show that the non-linear terms can be quite large, and the lateral friction is also seen to be non-negligible. A quasi-Sverdrupian regime is observed in the 60-280°E Southern Ocean section (Approximately excluding the Atlantic Sector), where the ACC drifts South. This overlaps with regions where deep mixed layers are found. Assessing the longitudinal area averaged vorticity terms, the BPT is seen to balance beta. Diagnosing the main momentum sinks, Hughes and Killworth (1995) connect the main ACC momentum sinks with bathymetric features of the Patagonian shelf, the Campbell Plateau and the Pacific-Antarctic Ridge. These are revealed as the ACC drifts north, with the togographic features inducing a pressure difference. Wells and de Cuevas (1995) demonstrate that the lateral friction can have a large impact, especially if the areas of the Drake passage and Scotia ridge are considered in a circumpolar average, suggesting that these areas are particularily important for dissipation of the wind input.

The steering effect of the $J(p_B, -H)$ term can be seen in its interaction with topography, with a vortex contraction (negative sign) as a flow hits an obstacle and a stretching (positive sign) as H deepens after the obstacle. The BPT term does not change greatly with resolution. However, large changes are seen in the partitioning of the baroclinic and barotropic (JEBAR) contributions to the term. The JEBAR term changes greatly with resolution, particularly in the Southern Ocean. This is likely the main source of the enhanced baroclinic anti-clockwise circulation in the Southern Ocean.

The link between the overturning and the PBT term is explored by Yeager (2015). The importance of the BPT term in the closure of the gyre and overturning circulation in the North Atlantic was highlighted. Yeager (2015) used 15 year integrations of a 1° and a 1/10° version of the POP2 model with 62 vertical levels. The study illustrates that the BPT term is dominant in the vorticity balance of the Atlantic meridional overturning circulation, representing a key link between the gyre and overturning circulation. The BPT term is found to act as the coupling between the large scale barotropic and baroclinic flows. The work we present here illustrates that these conjectures can be applied globally, and that the Southern Ocean is particularily sensitive to the topographic coupling through the baroclinic component of the BPT term.

Nikurashin *et al.* (2013) discuss ways energy is dissipated in geostrophic flows, also highlighting the importance of the Southern Ocean as the primary location of wind power input, where the westerly winds are aligned with the ACC. This creates a store of potential energy, which is released through baroclinic instabilities in a vigorous geostrophic eddy field. The focus on the baroclinic component of the circulation implies a sensitivity to resolution through the ∇H term found in the BPT term. This fits very well the present study, with the barotropic contribution being increasingly influential as the resolution increases towards allowing a mesoscale eddy field to develop. LaCase and Isachsen (2010) summarizes the conventional understanding that eddies provide the mechanism for meridional transport in the ACC. The results presented here in terms of the strengthening of the baroclinic contribution to the overturning is a natural conjecture. The sensitivity to resolution demonstrated in the baroclinic contribution to the BPT term follows, in line with work concentrating on the North Atlantic (Yeager 2015).

Jackson *et al.* (2006) investigated the role of bathymetric control on basin and channel flows, assessing the role of BPT and friction. In this work, friction is not explored explicitly, and conjectures borrowed from Jackson *et al.* (2006). Hughes and de Cuevas (2001) shows that the return flow in a WBC in the presence of sloping sidewalls is independent of friction, meaning that the role of friction is negligible in enabling the return flow in a wind-driven barotropic vorticity generalization of Sverdrup balance. This is counterintuitive, as it is also widely accepted that friction is important for the potential vorticity balance and ensuring a closed circulation. This contrast between the potential vorticity balance and the barotropic vorticity balance is intuitive in idealized flat bottom scenarios with vertical sidewalls where the two balances are identical. Jackson *et al.* (2006) shows how the balances change when topography and stratification are introduced. They show that along a western boundary the BPT returns the wind driven transport across latitude lines. Friction is only important in altering the potential vorticity within an isopycnal layer, allowing a closed circulation. To illustrate, when the subtropical jet separates from the western wall there are opposing frictional torques on either side of the jet, which cancel in a zonal integral of the barotropic vorticity, but alter the layer potential vorticity. This changes in a channel flow scenario like the Southern Ocean, where the BPT acts to transfer barotropic vorticity from the neighbouring gyres into the zonal jet, as well as returning the wind-driven flows along the western boundaries of the partial togographic barriers. In the present work, the depth-integrated flow which is steered by topography is what controls where the bottom friction alters the potential vorticity. In this manner, different potential vorticity states can be attained in separate sub-basins along the channel.

In summary, the change in the partitioning of the baroclinic (JEBAR) and barotropic part of the BPT illustrates an increase in the importance of the baroclinic topographic interactions with resolution. Our results suggest that this is what gives rise to the increased baroclinic contribution to the overturning, seen in the 30 year mean overturning. This has implications for the balance of forces, suggesting that significant changes can take place when the resolution increases. The changes with resolution of interactions with topography in terms of vortex stretching was found mainly in the baroclinic JEBAR component.

5. Acknowledgements

This work was funded by the EPSRC Doctoral Training Centre grant (EP/G03690X/1).

APPENDIX

A1. JEBAR derivation

Expressing JEBAR $f(\mathbf{u}_{gb} - \overline{\mathbf{u}}_g) \cdot \nabla H$ in terms of the baroclinic structure, the geostrophic balance in the meridional momentum equation is used:

$$-f\mathbf{u} = -\frac{p_x}{\rho_0}, \tag{A1}$$

$$\Rightarrow -f\overline{\mathbf{u}} = -\frac{1}{H}\int_{-H}^{0} \frac{p_x}{\rho_0} dz. \tag{A2}$$

Here A2 is the vertical average (denoted by the overbar) of the geostrophic balance in A1. Now we use the hydrostatic approximation:

$$p = p_b - \int_{-H}^{z} g\rho dz', \tag{A3}$$

$$\Rightarrow -f\overline{\mathbf{u}} = -\frac{1}{\rho_0} p_{bx} + \frac{1}{\rho_0 H}\frac{\partial}{\partial x}\int_{-H}^{0}\int_{-H}^{z} g\rho dz' dz, \tag{A4}$$

integration by parts gives us:

$$-f\overline{u} = -\frac{1}{\rho_0} p_{bx} + \frac{1}{\rho_0 H}\frac{\partial}{\partial x}\left[-\int_{-H}^{0} zg\rho dz' + \left[z\int_{H}^{z} g\rho dz'\right]_{-H}^{0}\right], \tag{A5}$$

which we re-write as:

$$-f\overline{\mathbf{u}} = -f\mathbf{u}_b - \frac{1}{H}\Phi_x, \tag{A6}$$

$$\Phi = \frac{g}{\rho_0}\int_{-H}^{0} z\rho dz. \tag{A7}$$

Where Φ is the potential energy per unit area.

we find the JEBAR term:

$$f(\mathbf{u}_{gb} - \overline{\mathbf{u}}_g)\cdot\nabla H = \frac{1}{H}J(\Phi, H), \tag{A8}$$

and so:

$$\frac{1}{\rho_0}J(p,H)_b = \frac{1}{H}J(\Phi,H) + f\overline{\mathbf{u}}_g \cdot \nabla H. \tag{A9}$$

References

Arakawa, A. and Lamb, V.R.: Computational design of the basic dynamical process of the UCLA general circulation model, Methods in Computational Physics, 17, Academic Press, New York, 173-265, 1977.

Barnier, B., Madec, G., Penduff, T., Molines, J.M., Treguier, A.M., Le Sommer, J., Beckmann, A., Biastoch, A., Bning, C., Dengg, J., Derval, C., Durand, E., Gulev, S., Remy, E., Talandier, C., Theetten, S., Maltrud, M., McClean, J., and De Cuevas, B.: Impact of partial steps and momentum advection schemes in a global ocean circulation model at eddy permitting resolution, Ocean Dynam., 56, 543-567, doi:10.1007/s10236-006-0082-1, 2006.

Bell, M.J.: Vortex stretching and bottom torques in the Bryan-Cox ocean circulation model, J. Geophys. Res., 104, 23545-23563, 1999.

Bourdallé-Badie, R., Treguier, A.M., Molines, J.M., Coward, A., Scheinert, M., Lu, Y., Lecointre, A. and Tranchant, B.: The ORCA12 bathymetry V3.2. Technical report, MERCATOR-DRAKKAR report, 2012.

Brodeau, L., Barnier, B., Treguier, A.M., Penduff, T. and Gulev, S.: An ERA40-based atmospheric forcing for global ocean circulation models, Ocean Modelling, 31 (3-4), 88-104, 2010.

fire Cane, M.A., Kamenkovich, V.M. and Krupitsky, A.: On the Utility and Disutility of JEBAR, J. Phys. Oceanogr., 28, 519-526. doi: `http://dx.doi.org/10.1175/1520-0485(1998)028<0519:OTUADO>2.0.CO;2`, 1998.

Coward, A. C.: The ORCA1 model bathymetry, `http://www.noc.soton.ac.uk/nemo/?page=bathyimages`, National Oceanography Centre, Southampton, UK, 2006.

Dewar, R.C., Lineweaver, C.H., Niven, R.K. and Regenauer-Lieb, K. (eds.), Beyond the Second Law, Understanding Complex Systems, DOI: 10.1007/978-3-642-40154-1_1, Springer-Verlag Berlin Heidelberg, 2014.

Döös, K., and Webb, D.J.: The Deacon cell and the other meridional cells of the Southern Ocean, J. Phys. Oceanogr., 24(2), 429-442, 1994.

Greatbatch, R.J., Fanning, A.F., Goulding, A.D. and Levitus, S.: A diagnosis of interpentadal circulation changes in the North Atlantic, J. Geophys. Res., 96 (C12), 22 009-22 023, 1991.

Griffies, S.M., Pacanowski, R.C. and Hallberg, R.W.: Spurious diapycnal mixing associated with advection in a z-coordinate ocean model, Mon. Wea. Rev., 128, 538-564, 2000.

Hewitt, H.T., Copsey, D., Culverwell, I.D., Harris, C.M., Hill, R.S.R., Keen, A.B., McLaren, A.J. and Hunke E.C.: Design and implementation of the infrastructure of HadGEM3: the next-generation Met Office climate modelling system, Geosci. Model Dev., 4 (2), 223-253, doi:10.5194/gmd-4-223-2011, 2011.

Hughes, C.W. and Killworth, P.D.: Effects of Bottom Topography in the Large-Scale Circulation of the Southern Ocean, J. Phys. Oceanogr., 25, 2485-2497, doi: `http://dx.doi.org/10.1175/1520-0485(1995)025<2485:EOBTIT>2.0.CO;2`, 1995.

Hughes, C.W. and de Cuevas, B.A.: Why western boundary currents in realistic oceans are inviscid: a link between form stress and bottom pressure torques, Journal of Physical Oceanography, 31 (10), 2871-2885. doi: `http://dx.doi.org/10.1175/1520-0485(2001)031<2871:WWBCIR>2.0.CO;2`, 2001.

IPCC: Climate Change 2013: The Physical Science Basis. Contribution of Working Group I to the Fifth Assessment Report of the Intergovernmental Panel on Climate Change [Stocker, T.F., D. Qin, G.K. Plattner, M. Tignor, S.K. Allen, J. Boschung, A. Nauels, Y. Xia, V. Bex and P.M. Midgley (eds.)]. Cambridge University Press, Cambridge, United Kingdom and New York, NY, USA, 1535 pp, doi:10.1017/CBO9781107415324, 2013.

LaCasce, J.H. and Isachsen, P.E. (2010). The linear models of the ACC. Progress in Oceanography. ISSN 0079-6611. 84(3-4), s 139- 157 . `doi:10.1016/j.pocean.2009.11.002`

Jackett, D.R. and McDougall, T.J.: Minimal adjustment of hydrographic data to achieve static stability, J. Atmos. Ocean Tech., 12, 381-389, 1995.

Jackson, L., Hughes, C.W. and Williams, R.G.: Topographic Control of Basin and Channel Flows: The Role of Bottom Pressure Torques and Friction, J. Phys. Oceanogr., 36, 1786-1805. doi: `http://dx.doi.org/10.1175/JPO2936.1`, 2006.

Lee, MM., Coward, A.C., and Nurser, A.J.G.: Spurious diapycnal mixing of the deep waters in an eddy-permitting global ocean model, Journal of Physical Oceanography, 32 (5), 1522-1535. 10.1175/1520-0485(2002)032¡1522:SDMOTD¿2.0.CO;2, 2002.

Luyten

Madec, G.: NEMO ocean engine, Note du Pole de modlisation, Institut Pierre-Simon Laplace (IPSL), 27, 2008.

Marsh, R., de Cuevas, B.A., Coward, A.C., Jacquin, J., Hirschi, J.J.M., Aksenov, Y., Nurser, A.J.G. and Josey, S.A.: Recent changes in the North Atlantic circulation simulated with eddy-permitting and eddy-resolving ocean models, Ocean Modelling 28(4), 226-239, url: `http://dx.doi.org/10.1016/j.ocemod.2009.02.007`, 2009.

Marzocchi, A., Hirschi, J.J.M., Penny, H.N., Cunningham, S.A., Blaker, A.T. and Coward, A.C.: The North Atlantic subpolar circulation in an eddy-resolving global ocean model, Journal of Marine Systems, 142, doi:126-143. 10.1016/j.jmarsys.2014.10.007, 2015.

Megann, A.P., Storkey, D., Aksenov, Y., Alderson, S., Calvert, D., Graham, T., Hyder, P., Siddorn, J. and Sinha, B.: GO 5.0: The joint NERC-Met Office NEMO global ocean model for use in coupled and forced applications, Geotechnical Model Development, 7 (3), 1069-1092, doi:10.5194/gmd-7-1069-2014, 2014.

Mertz, G. and Wright, D.G.: Interpretations of the JEBAR Term, J. Phys. Oceanogr., 22, 301-305, doi: `http://dx.doi.org/10.1175/1520-0485(1992)022<0301:IOTJT>2.0.CO;2`, 1992.

Munk, W., 1950: On the wind-driven ocean circulation. J. Meteor., 7, 7993, doi:10.1175/1520-0469(1950)007¡0080:OTWDOC¿2.0.CO;2.

Munk, W.H., and Palmén, E,: Note on the dynamics of the Antarctic Circumpolar Current, Tellus, 3, 53-55, 1940.

Myers, P.G., Fanning, A.F. and Weaver, A.J.: JEBAR, Bottom Pressure Torque, and Gulf Stream Separation, J. Phys. Oceanogr., 26, 671-683, doi: `http://dx.doi.org/10.1175/1520-0485(1996)026<0671:JBPTAG>2.0.CO;2`, 1996.

Naveira Garabato, A.C., Nurser, A.J.G., Scott, R.B. and Goff, J.A.: The Impact of Small-Scale Topography on the Dynamical Balance of the Ocean, J. Phys. Oceanogr., 43, 647-668. doi: `http://dx.doi.org/10.1175/JPO-D-12-056.1`, 2013.

Nikurashin, M., Vallis, G.K. and Adcroft, A.: Routes to Energy Dissipation for Geostrophic Flows in the Southern Ocean, Nature Geosci 6, 1, 48-51, 2013.

Nurser, G.A. and Lee, M.M.: Isopycnal Averaging at Constant Height. Part II: Relating to the Residual Streamfunction in Eulerian Space, J. Phys. Oceanogr., 34, 2740-2755, doi: `http://dx.doi.org/10.1175/JPO2650.1`, 2004.

Pedlowski, J.: Geophysical Fluid Dynamics, Springer, 1979.

Penduff, T., Barnier, B., Verron, J., Kerbiriou, M.A.: How topographic smoothing contributes to differentiating the eddy flows simulated by sigma- and z-level models, J. Phys. Oceanogr., 32, 122-137, 2002.

Sarkisyan, A.S., and Ivanov, V.F.: The combined effect of baroclinicity and bottom relief as an important factor in the dynamics of ocean current, Izv. Acad. Sci. USSR Atmos. Oceanic Phys., Engl. Transl.,1, 173-188, 1971.

Scaife, A. A., Copsey, D., Gordon, C., Harris, C., Hinton, T., Keeley, S., ONeill, A., Roberts, M., and Williams, K.: Improved Atlantic winter blocking in a climate model, Geophys. Res. Lett., 38, L23703, doi:10.1029/2011GL049573, 2011.

Schoonover, J., Dewar, W., Wienders, N., Gula, J., McWilliams, J.C., Molemaker, M.J., Bates, S.C., Danabasoglu, G. and Yeager, S.: North Atlantic Barotropic Vorticity Balances in Numerical Models, Journal of Physical Oceanography 2016 46:1, 289-303

Stommel, H. (1948), The westward intensification of wind-driven ocean currents, Eos Trans. AGU, 29(2), 202206, doi:10.1029/TR029i002p00202.

Stommel, H., and Arons, A.B.: On the abyssal circulation of the world ocean. Part I: Stationary planetary patterns on a sphere. Deep-Sea Res.,6, 140-154, 1960a.

Stommel, H. and Arons, A.B.: On the abyssal circulation of the world ocean. Part II: An idealized model of the circulation pattern and amplitude in oceanic basins. Deep-Sea Res.,6, 217-233, 1960b.

Sverdrup, H.: Wind-driven currents in a baroclinic ocean; with application to the equtorial currents of the eastern Pacific, Proc. Natl. Acad. Sci. (USA), 33, 318-326, 1947.

Thomas, L.N.: Formation of intrathermocline eddies at ocean fronts by wind-driven destruction of potential vorticity, Dynam. Atmos. Oceans, 45, 252-273, 2008.

Thomas, M.D., De Boer, A.M., Johnson, H.L. and Stevens, D.P.: Spatial and Temporal Scales of Sverdrup Balance, J. Phys. Oceanogr., 44, 2644-2660. doi: http://dx.doi.org/10.1175/JPO-D-13-0192.1, 2014.

Wells, N.C. and De Cuevas, B.A.: Depth-Integrated Vorticity Budget of the Southern Ocean from a General Circulation Model, J. Phys. Oceanogr., 25, 2569-2582. doi: http://dx.doi.org/10.1175/1520-0485(1995)025<2569:DIVBOT>2.0.CO;2, 1995.

Wunsch, C.: The decadal mean ocean circulation and Sverdrup balance, J. Mar. Res. 69, 417-434, 2011.

Yeager, S.: Topographic coupling of the Atlantic overturning and gyre circulations, J. Phys. Oceanogr., 45, 1258-1284. doi: http://dx.doi.org/10.1175/JPO-D-14-0100.1, 2015.

Zika, J.D., England, M.H. and Sijp, W.P.: The Ocean Circulation in Thermohaline Coordinates, Journal of Physical Oceanography, 2, 708-724, 2012.

LIST OF TABLES

Name	ORCA1-N406	ORCA025-N401	ORCA0083-N01
Resolution	1°	1/4°	1/12°
z, x, y	75,292,362	75,1021,1442	75,3059,4322
GM active	Yes	No	No
Horiz. laplacian eddy viscosity (m^2s^{-1})	10^4	500	500
Horiz. bilaplacian eddy viscosity (m^4s^{-1})	-1.25×10^{10}	-2.2×10^{11}	-2.2×10^{11}
Lateral eddy tracer diffusivity (m^2s^{-1})	10^3	300	125
Timestep (s)	3600	1440	200

TABLE 1: Changes with resolution in configuration of NEMO. The vertical resolution (z) is at 75 vertical levels throughout the experiments.

LIST OF FIGURES

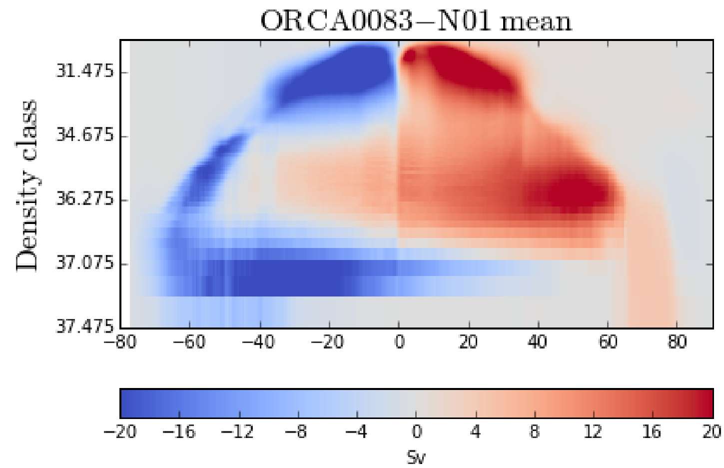

(a) ORCA0083-N01 mean, full

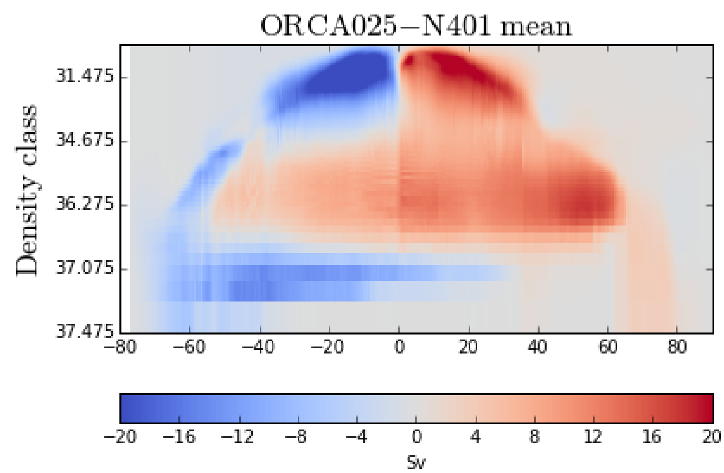

(b) ORCA025-N401 mean, full

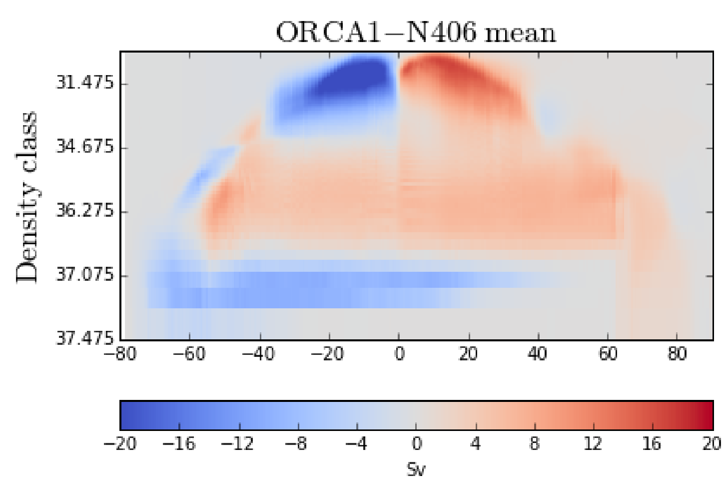

(c) ORCA1-N406 mean, full

FIG. 1: The global overturning $\Psi_{\sigma y}$ in ρ space (Sv), showing the mean circulation from the 1978 to 2007 time series. To highlight the deep watermasses, we are using a logarithmically stretched sigma coordinate. We crop the bottom of the plot where it goes to zero.

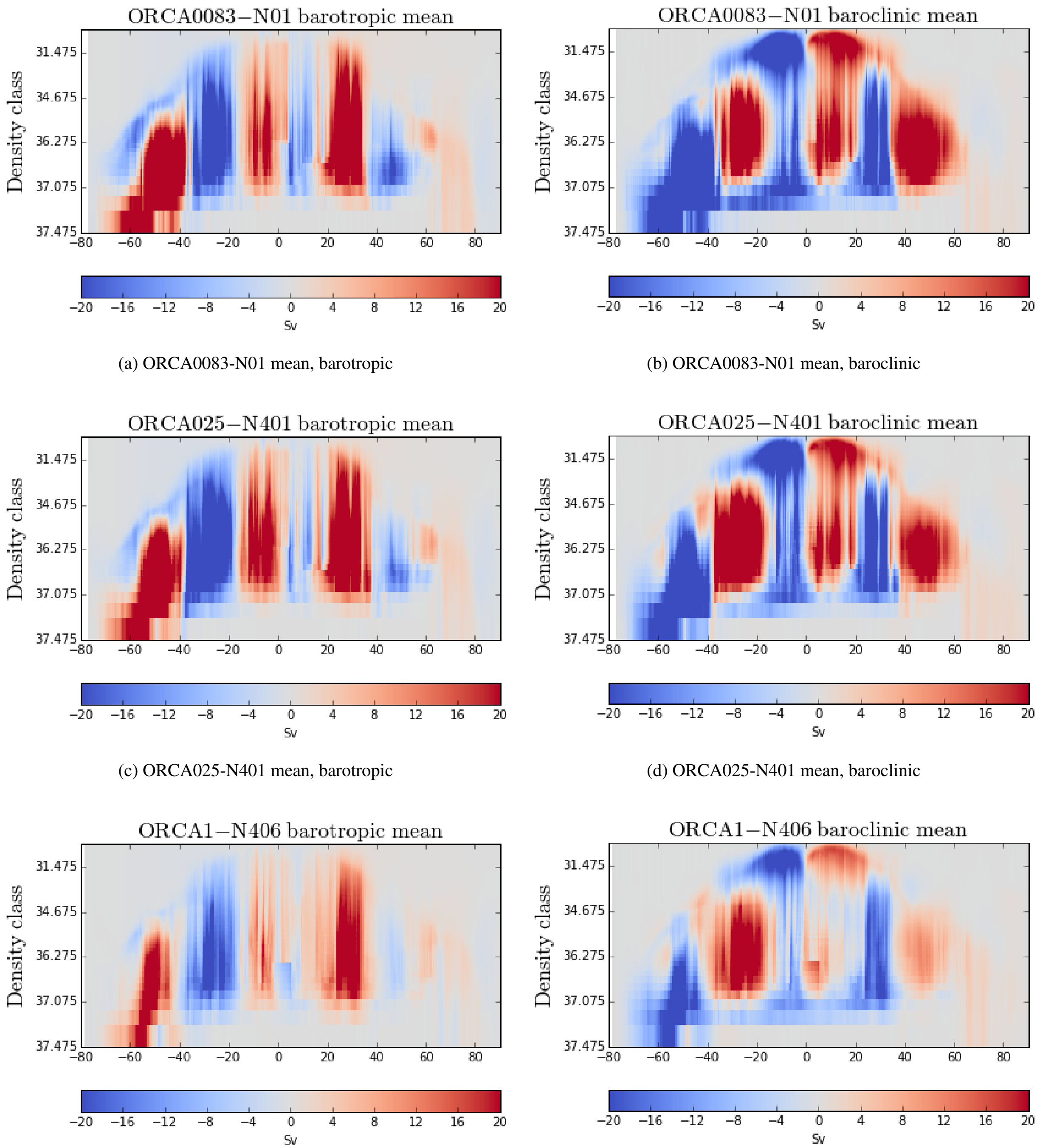

(a) ORCA0083-N01 mean, barotropic

(b) ORCA0083-N01 mean, baroclinic

(c) ORCA025-N401 mean, barotropic

(d) ORCA025-N401 mean, baroclinic

(e) ORCA1-N406 mean, barotropic

(f) ORCA1-N406 mean, baroclinic

FIG. 2: The global overturning cell in ρ space (Sv). Showing the mean barotropic and baroclinic circulation from the 1978 to 2007 time series. To highlight the deep watermasses, we are using a logarithmically stretched sigma coordinate. We crop the bottom of the plot, where it goes to zero.

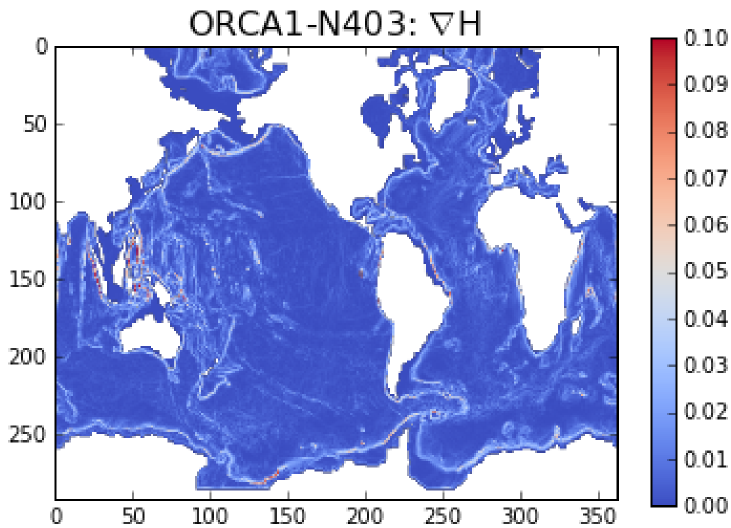

(a) ORCA1-N403, ∇H

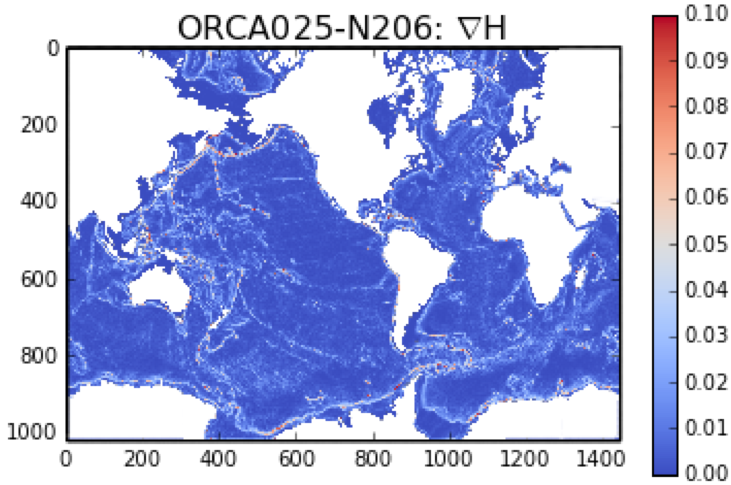

(b) ORCA025-N401, ∇H

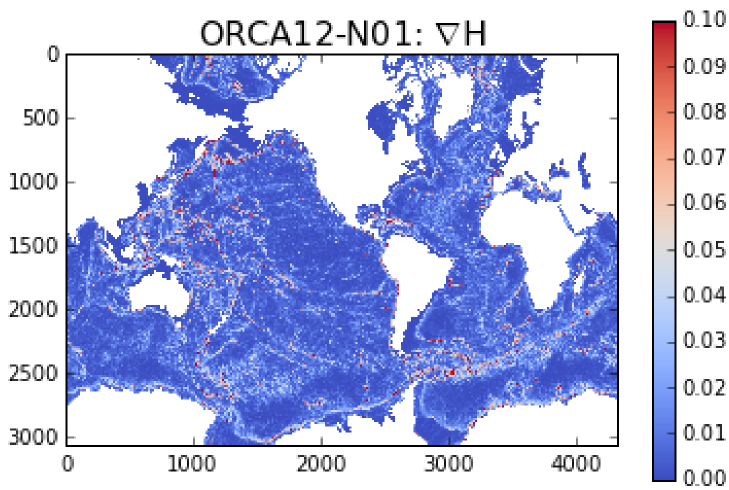

(c) ORCA0083-N01, ∇H

FIG. 3: The ∇H term in ORCA0083-N01, ORCA025-N205 and ORCA1-N406, scaled between 0 and 0.1. Note the increase in roughness with resolution.

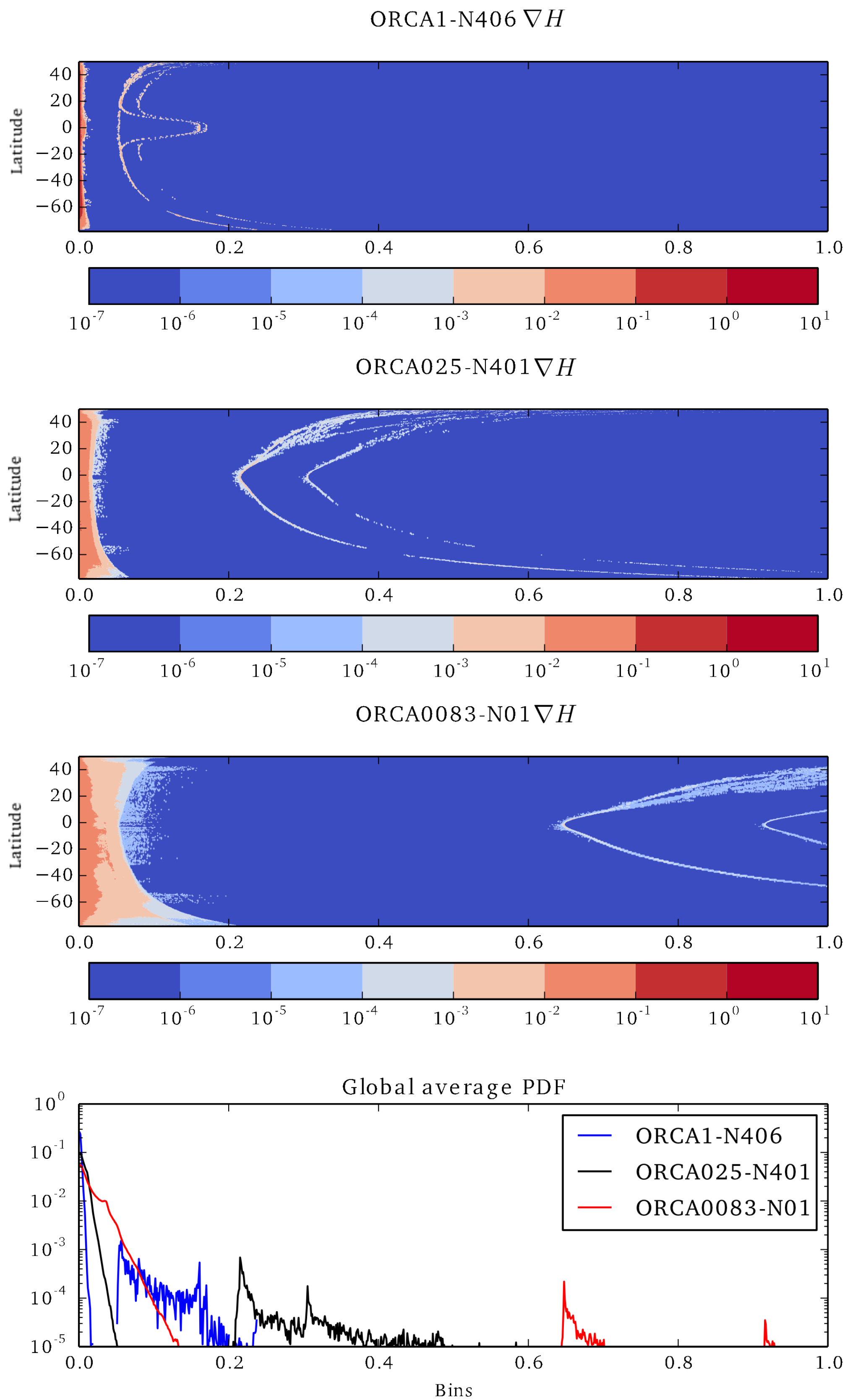

FIG. 4: The Probability Density Function for ∇H. Bins are for ∇H scaled between 0 and 1. The top three plots show the latitudinal PDFs for ORCA1, ORCA025 and ORCA0083 respectively from the top. The lower panel shows the global PDF. Note the increase in roughness with resolution.

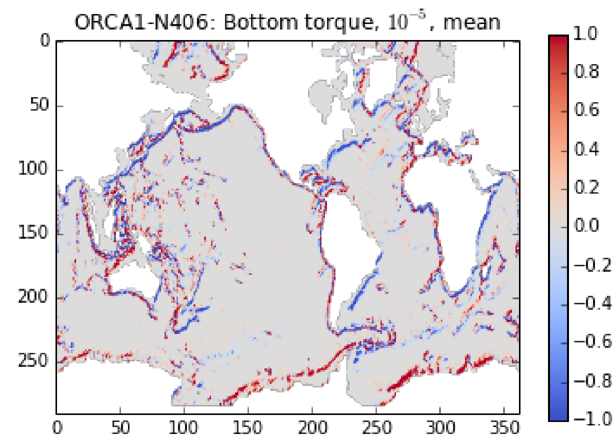

(a) ORCA1, BPT

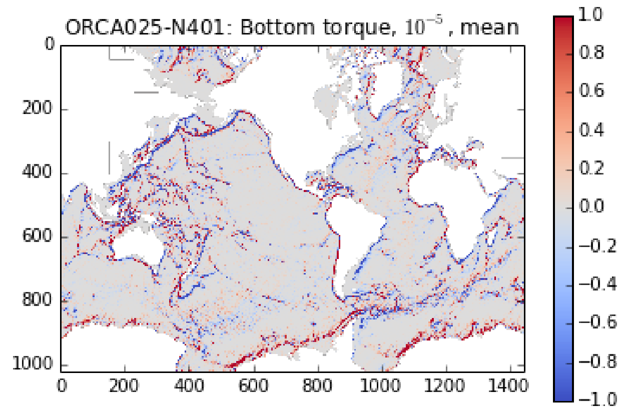

(b) ORCA025, BPT

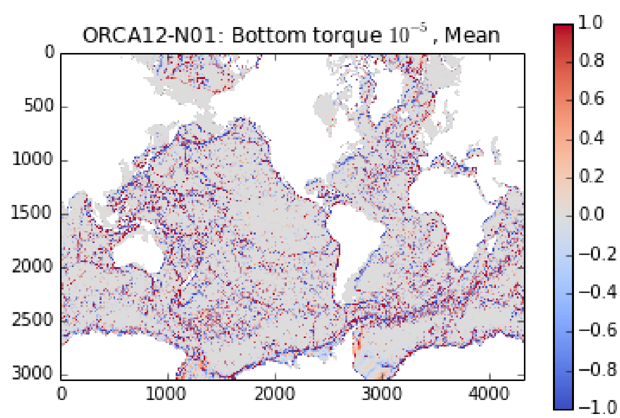

(c) ORCA12, BPT

FIG. 5: The bottom torque term in ORCA0083, ORCA025 and ORCA1 for 30 year mean.

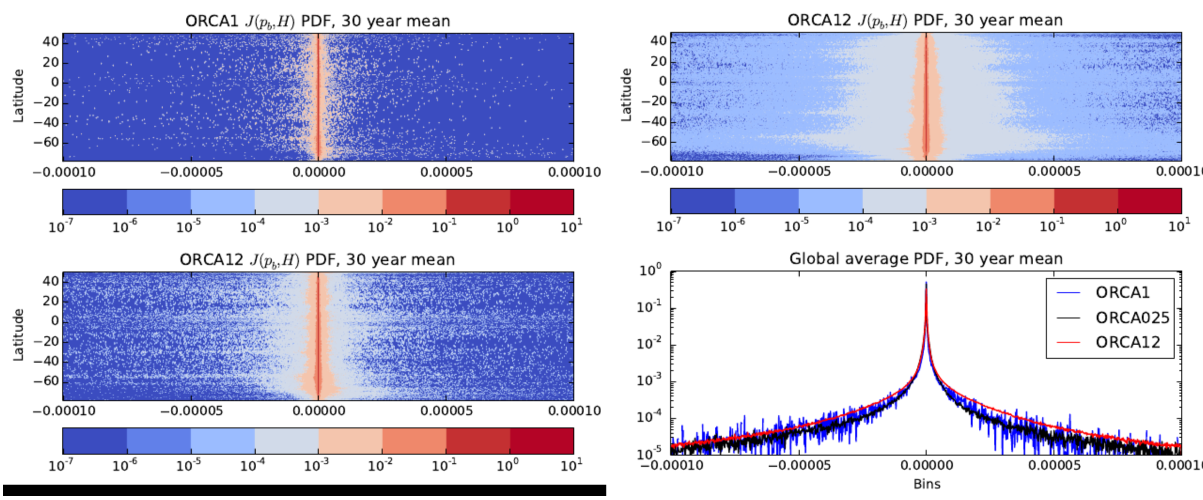

FIG. 6: The Probability Density Function for bottom pressure torque, 30 year mean.

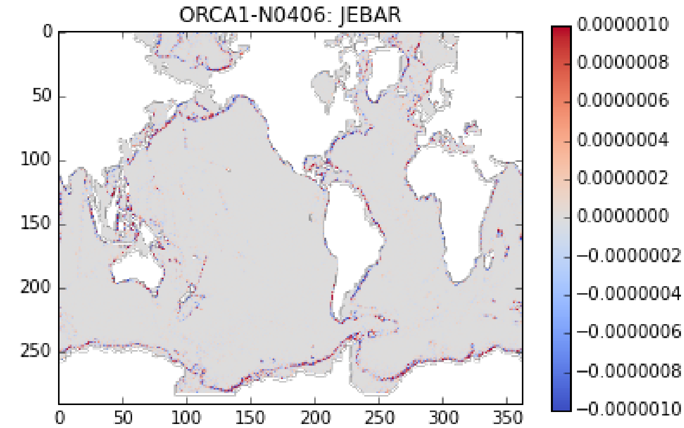

(a) ORCA1-N406, JEBAR

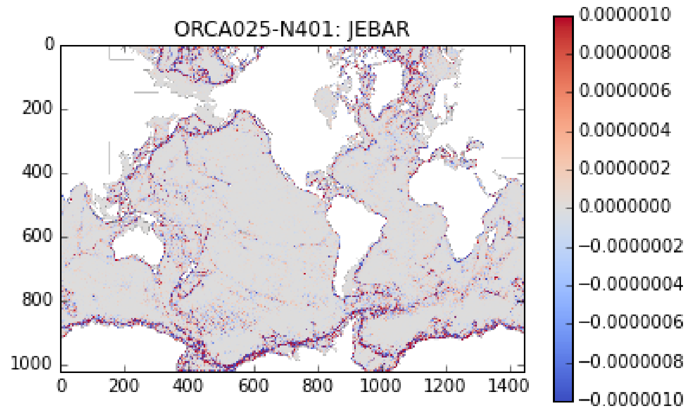

(b) ORCA025-N401, JEBAR

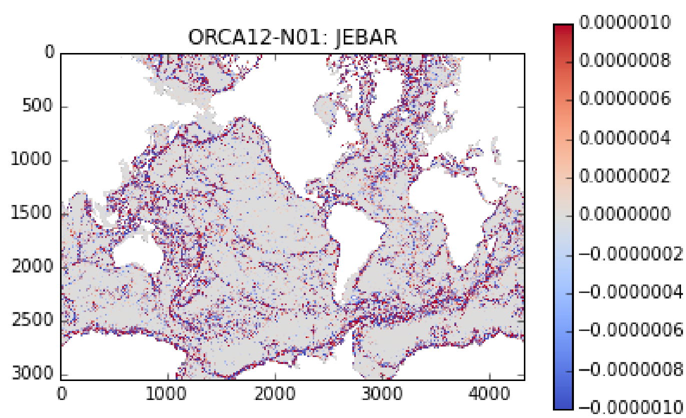

(c) ORCA12-N01, JEBAR

FIG. 7: The JEBAR term in ORCA0083-N01, ORCA025-N401 and ORCA1-N406.

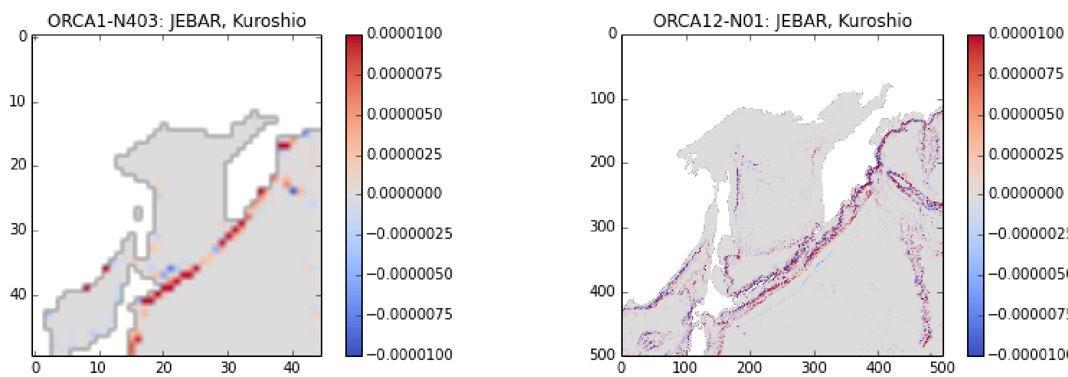

(a) ORCA1-N403, Pass1, JEBAR

(b) ORCA12-N01 JEBAR

FIG. 8: The JEBAR term in ORCA0083-N01 and ORCA1-N403, detail from the northern Japan/Kamtchatka region.

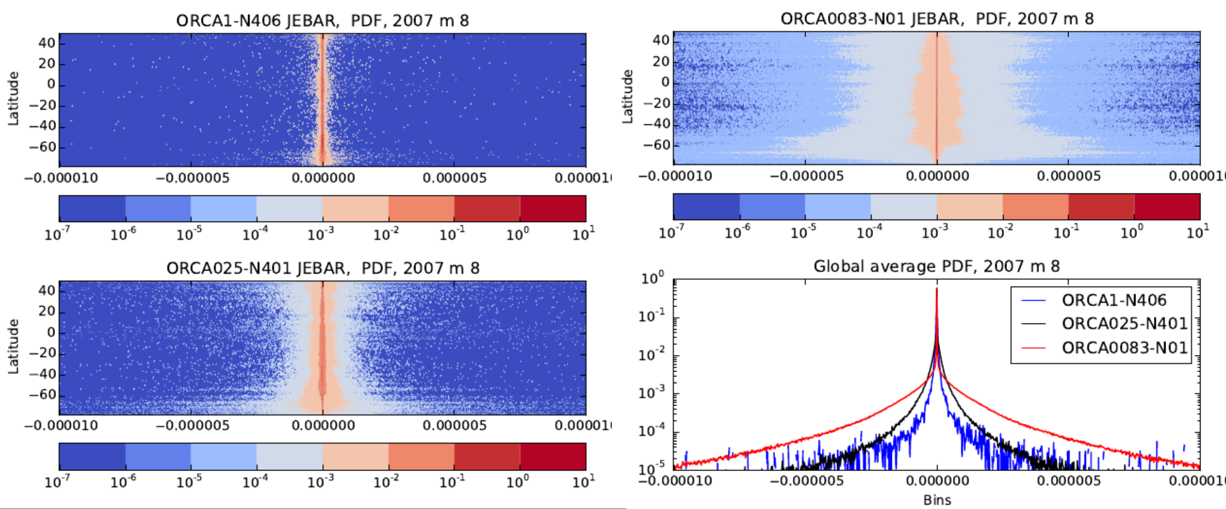

FIG. 9: PDF of latitudinally averaged and global averaged JEBAR, ORCA0083-N01 (red line), ORCA025-N401 (black line) and ORCA1-N406 (blue line).